

Scattering of inhomogeneous circularly polarized optical field and mechanical manifestation of the internal energy flows

A. Ya. Bekshaev^{1*}, O. V. Angelsky², S. G. Hanson³, and C. Yu. Zenkova²

¹ *I.I. Mechnikov National University, Dvorianska 2, Odessa 65082, Ukraine*

² *Chernivtsi National University, Kotsyubinsky Str. 2, Chernivtsi 58012, Ukraine*

³ *DTU Fotonik, Department of Photonics Engineering, DK-4000 Roskilde, Denmark*

Basing on the Mie theory and on the incident beam model via superposition of two plane waves, we analyze numerically the momentum flux of the field scattered by a spherical microparticle placed within the spatially inhomogeneous circularly polarized paraxial light beam. The asymmetry between the forward- and backward-scattered momentum fluxes in the Rayleigh scattering regime is revealed that appears due to the spin part of the internal energy flow in the incident beam. The transverse ponderomotive forces exerted on dielectric and conducting particles of different sizes are calculated, and special features of the mechanical actions produced by the spin and orbital parts of the internal energy flow have been recognized. In particular, the transverse orbital flow exerts on a subwavelength particle the transverse force that grows as a^3 for conducting and as a^6 for dielectric particle with radius a , in compliance with the dipole mechanism of the field-particle interaction; the force associated with the spin flow behaves as a^8 in both cases, which testifies for the non-dipole mechanism. The results can be used for experimental identification and separate investigation of the spin and orbital parts of the internal energy flow in light fields.

Keywords: optical field, spatial inhomogeneity, Poynting vector, spin energy flow, orbital energy flow, probe particle, mechanical action

PACS: 42.50.Wk, 42.25.Fx, 42.25.Ja, 42.60.Jf

I. INTRODUCTION

The steady interest to light beams with angular momentum and to singular optics [1–4] has stimulated growing attention to the internal energy flows in light fields (optical currents) [5–12]. The internal energy flow pattern provides a physically meaningful and universal characterization of arbitrary light fields. It is especially suitable for the near-field optics and in new applications associated with micro- and nanooptics, invisibility cloaking, superlensing and metamaterials [13–16]. But more important is that the internal energy flows help to disclose the intimate geometric and dynamic essentials of the light field transformations that underlies any process of a light beam formation, propagation or diffraction [9–12,17]. In particular, the total energy flow density (TFD), represented via the time-average Poynting vector distribution, can be subdivided into the “spin” (SFD) and “orbital” (OFD) parts to reflect the peculiar properties associated with the spin and orbital degrees of freedom of light, their distinguishing features and interrelations [9–12]. The spin

* E-mail: bekshaev@onu.edu.ua

flow is usually associated with inhomogeneous circular polarization while the orbital one owes to the explicit energy redistribution within an optical beam.

In view of such important and useful properties, the TFD as well as its spin and orbital constituents appear to be valuable instruments for the light field description and analysis. However, wide utilization of these instruments is hampered by difficulties in their experimental detection (visualization) and measurement. As far as we can judge, the only regular way of the energy flow measurement relies upon determining the electric and, if necessary, magnetic vectors of the optical field followed by the Poynting vector calculation via the standard formulas [13,18,19]. In this situation, possibilities for immediate detection and/or visualization of the internal flows become rather attractive and appealing. The most promising approach, repeatedly used in experimental practice [20–23], is based on the mechanical action the energy flow exerts on probe particles with various sizes, shapes and optical properties. It relies on the fact the TFD is proportional to the field momentum density [24], and on the assumption that a particle, due to absorption, reflection or scattering of the incident light, accepts partially the light field momentum and starts to move in accordance with its local value and direction. During the past years, this approach has been well elaborated, mainly due to close connection with problems of optically driven micro-machines, micro-engineering and micromanipulation [20,25].

Nevertheless, despite many impressive practical results, in application to the fundamental study of the internal flows this method is still far from ideal. The main reason is that the field-induced motion of particles depends on many additional factors: together with the electromagnetic ponderomotive influences of non-Poynting origin (gradient force, dissipative force, polarization-dependent dipole force [26–29]), the specific ghost effects may occur due to the medium in which the probe particles are suspended (radiometric, photophoretic forces, the medium viscosity, etc.), the particle-containing cell (its configuration, the wall friction) and because of the particle shape and material [20,25]. Even in situations where all non-Poynting sources are isolated (e.g., due to special geometry of the field and the measuring equipment [20,26] or by proper calibration procedures), it is rather difficult to establish an exact numerical correspondence between the probe particle motion and the local value of the field momentum. First, there is no simple and transparent model of a force produced by the electromagnetic momentum interacting with a medium [10], and second, any particle disturbs the electromagnetic field in the ambient region, of at least the wavelength-order size, and the real field “felt” by the particle may be very different from the “incident” field pattern that existed before the particle was placed there [12,30,31].

The situation is further complicated by the existence of two sorts of the energy flow with different nature. The mechanical action of the OFD can be fairly explained by using the notion of transverse light pressure [12]. At the same time, although the SFD’s ability to cause translation or orbital motion of particles has been proved both by simulation [26] and in experiment [32,33], the physical nature of this effect cannot be understood on the base of existing model of the SFD genesis [3,7]. Moreover, the usual model of the optical force acting on a subwavelength-size particle (in the Rayleigh scattering regime), which is based on the classical dipole-interaction Hamiltonian [28,34], does not predict any force associated with the SFD. In these circumstances, the question arises on the nature of the SFD-induced mechanical action and on the mechanical equivalence between the OFD and the SFD: whether the spin and orbital momenta produce the same motion of a particle, provided that they possess the same direction and magnitude?

In our opinion, a possible way of resolving the above problems and questions can be found in considering relatively simple model situations where relations between the force acting on a particle and the energy flow in the incident optical field can be easily calculated and interpreted, so that contributions of the spin and orbital energy flow constituents can be “isolated” and studied separately. An example of such an approach was described recently [26]: the incident field is formed by only two plane waves, which allows one to employ the standard Mie theory for calculation of the field mechanical action. Then the results are juxtaposed with the TFD, OFD and

SFD patterns of the incident field, as well as with its energy distribution. This enables to identify the ponderomotive contributions owing to the different energy flow constituents together with the influences of the non-Poynting factors, with explicit account for the field structure and the particle's optical properties. Despite the simplicity, this model is flexible enough to represent main features of fields with inhomogeneous distributions of the amplitude, phase and polarization that can be realized in experiment [27]. In this work, within the frame of that model, we “construct” the field configurations that distinctly differ by the SFD and OFD patterns and analyze the mechanical actions they exert on dielectric and absorbing particles. This allows us to reveal some special features of the ponderomotive influences associated with the different kinds of the field momentum, their similar and distinguishing aspects, and to discuss possibilities for practical detection of the internal energy flows and discrimination between their spin and orbital constituents.

II. MODEL DESCRIPTION

A. Incident field

In what follows, we will consider monochromatic optical waves where the electric and magnetic vectors can be written in forms $\text{Re}[\mathbf{E}\exp(-i\omega t)]$, $\text{Re}[\mathbf{H}\exp(-i\omega t)]$ with complex amplitudes \mathbf{E} and \mathbf{H} . Then the time-average Poynting vector distribution \mathbf{S} representing the field TFD and the field momentum density \mathbf{p} are determined by expression [24]

$$\mathbf{S} = c^2 \mathbf{p} = gc \text{Re}(\mathbf{E}^* \times \mathbf{H}). \quad (1)$$

Here $g = (8\pi)^{-1}$ in the Gaussian system of units, c is the light velocity in vacuum. Due to proportionality between \mathbf{S} and \mathbf{p} it would be convenient to operate only one of these quantities in further discussion; we choose \mathbf{p} though preserving the name “energy flow density” for its physical meaning. In further consideration we shall take into account that the field-particle interaction takes place in a medium rather than in vacuum; then \mathbf{p} in Eq. (1) represents the kinetic (Abraham) momentum density of the electromagnetic field, and its decomposition into the spin and orbital parts, \mathbf{p}_s and \mathbf{p}_o , reads [35]

$$\mathbf{p}_s = \frac{g}{4\omega} \text{Im} \left[\nabla \times \left(\frac{1}{\mu} \mathbf{E}^* \times \mathbf{E} \right) + \nabla \times \left(\frac{1}{\varepsilon} \mathbf{H}^* \times \mathbf{H} \right) \right], \quad (2)$$

$$\begin{aligned} \mathbf{p}_o &= \mathbf{p} - \mathbf{p}_s \\ &= \frac{g}{2\omega} \text{Im} \left[\frac{1}{\mu} \mathbf{E}^* \cdot (\nabla) \mathbf{E} - \frac{1}{2} \nabla \left(\frac{1}{\mu} \right) \times (\mathbf{E}^* \times \mathbf{E}) + \frac{1}{\varepsilon} \mathbf{H}^* \cdot (\nabla) \mathbf{H} - \frac{1}{2} \nabla \left(\frac{1}{\varepsilon} \right) \times (\mathbf{H}^* \times \mathbf{H}) \right], \end{aligned} \quad (3)$$

where ε and μ are the medium permittivity and permeability, $\mathbf{E}^* \cdot (\nabla) \mathbf{E}$ is the invariant notation for the vector operation that in Cartesian components reads [10,12]

$$\mathbf{E}^* \cdot (\nabla) \mathbf{E} = E_x^* \nabla E_x + E_y^* \nabla E_y + E_z^* \nabla E_z.$$

Eqs. (2) and (3) are written for general conditions admitting the medium inhomogeneity; in a homogeneous case, Eq. (3) can be easily simplified omitting the terms with gradients of ε^{-1} and μ^{-1} . Another important quantity that plays a substantial role in further analysis is the time-average energy density

$$w = \frac{g}{2} (\varepsilon |\mathbf{E}|^2 + \mu |\mathbf{H}|^2). \quad (4)$$

Following to Ref. [26], our task is to determine the electromagnetic field disturbed by the presence of a particle, to calculate its momentum and to compare the result with the initial momentum carried by the “pure” incident field. In general, due to the particle presence, the scattered field \mathbf{E}_{sc} , \mathbf{H}_{sc} emerges that should be added to the incident field \mathbf{E} , \mathbf{H} [31] so the total field momentum density is changed by

$$\mathbf{H}_{aj}(x, y_j, z_j) \equiv \mathbf{H}_j \exp(ikz_j) = \sqrt{\frac{\varepsilon}{\mu}} \mathbf{e}_j \times \mathbf{E}_{aj}(z_j) \quad (8)$$

where E_{xj} and E_{yj} are constants, \mathbf{e}_j is the unit vector of the z_j -axis and $k = n\omega/c$ is the wave number of the incident radiation in the medium. The optical field distribution, created by waves (8) in the common reference plane $z = 0$, is generally inhomogeneous and in the laboratory coordinates can be written in the form

$$\mathbf{E}_{aj}(x, y) = \begin{pmatrix} E_{xj} \\ E_{yj} \cos \gamma_j \\ -E_{yj} \sin \gamma_j \end{pmatrix} \exp(ikz_j), \quad \mathbf{H}_{aj}(x, y) = \sqrt{\frac{\varepsilon}{\mu}} \begin{pmatrix} -E_{yj} \\ E_{xj} \cos \gamma_j \\ -E_{xj} \sin \gamma_j \end{pmatrix} \exp(ikz_j) \quad (9)$$

where z_j is related to y and z by the first Eq. (6).

In the present paper, we are restricted to the case where the superposition consists of only two plane waves ($j = 1, 2$), and the electric and magnetic strengths of the incident optical field equal to

$$\mathbf{E} = \mathbf{E}_{a1} + \mathbf{E}_{a2}, \quad \mathbf{H} = \mathbf{H}_{a1} + \mathbf{H}_{a2}. \quad (10)$$

Operating similarly to Ref. [26], one finds the field energy density (4) as well as the SFD (2) and OFD (3) components:

$$w = \varepsilon g \left[|\mathbf{E}_1|^2 + |\mathbf{E}_2|^2 + \cos^2 \frac{\gamma_1 - \gamma_2}{2} D(y, z) \right]; \quad (11)$$

$$p_{sx} = \frac{g_e}{2c} \sin(\gamma_1 - \gamma_2) \left[(E_{x2}^* E_{y1} - E_{y2}^* E_{x1}) e^{ik(z_1 - z_2)} + (E_{y1}^* E_{x2} - E_{x1}^* E_{y2}) e^{ik(z_2 - z_1)} \right], \quad (12)$$

$$p_{sy} = \frac{g_e}{2c} \sin^2 \frac{\gamma_1 - \gamma_2}{2} (\sin \gamma_1 + \sin \gamma_2) D(y, z), \quad (13)$$

$$p_{sz} = \frac{g_e}{2c} \sin^2 \frac{\gamma_1 - \gamma_2}{2} (\cos \gamma_1 + \cos \gamma_2) D(y, z); \quad (14)$$

$$p_{ox} = 0, \quad (15)$$

$$p_{oy} = \frac{g_e}{c} \left[|\mathbf{E}_1|^2 \sin \gamma_1 + |\mathbf{E}_2|^2 \sin \gamma_2 + \frac{1}{2} \cos^2 \frac{\gamma_1 - \gamma_2}{2} (\sin \gamma_1 + \sin \gamma_2) D(y, z) \right], \quad (16)$$

$$p_{oz} = \frac{g_e}{c} \left[|\mathbf{E}_1|^2 \cos \gamma_1 + |\mathbf{E}_2|^2 \cos \gamma_2 + \frac{1}{2} \cos^2 \frac{\gamma_1 - \gamma_2}{2} (\cos \gamma_1 + \cos \gamma_2) D(y, z) \right] \quad (17)$$

where

$$g_e = g \sqrt{\frac{\varepsilon}{\mu}}, \quad D(y, z) = (E_{x2}^* E_{x1} + E_{y2}^* E_{y1}) e^{ik(z_1 - z_2)} + (E_{x1}^* E_{x2} + E_{y1}^* E_{y2}) e^{ik(z_2 - z_1)}. \quad (18)$$

Eqs. (11) – (18) show that the simple superposition of Eqs. (10) can serve a model of a rather general inhomogeneous field with non-zero spin and orbital flows [26]. Note that in the considered field geometry, due to Eqs. (16) and (17), x -component of the OFD is absent and the whole x -directed flow is of the spin nature (12).

B. Scattered field and mechanical action

The light scattered by a spherical particle illuminated by a plane monochromatic wave can be calculated with using the Mie theory [31,36]. To find the field mechanical action (5), one should know the scattered field at $R \rightarrow \infty$. For such conditions, the scattered field produced by the j -th plane wave (9) can be found via relations

$$\mathbf{E}_{scj} = \frac{e^{ikR}}{-ikR} \mathbf{E}_{sj}, \quad \mathbf{H}_{scj} = \frac{e^{ikR}}{-ikR} \mathbf{H}_{sj} \quad (19)$$

where

$$\begin{aligned}\mathbf{E}_{sj} &= \begin{pmatrix} E_{\theta sj} \\ E_{\phi sj} \end{pmatrix} = \begin{pmatrix} S_2 & 0 \\ 0 & S_1 \end{pmatrix} \begin{pmatrix} E_{\theta j} \\ E_{\phi j} \end{pmatrix} = \begin{pmatrix} S_2 & 0 \\ 0 & S_1 \end{pmatrix} \begin{pmatrix} E_{xj} \cos \phi_j + E_{yj} \sin \phi_j \\ -E_{xj} \sin \phi_j + E_{yj} \cos \phi_j \end{pmatrix}, \\ \mathbf{H}_{sj} &= \begin{pmatrix} H_{\theta sj} \\ H_{\phi sj} \end{pmatrix} = \sqrt{\frac{\varepsilon}{\mu}} \begin{pmatrix} 0 & -1 \\ 1 & 0 \end{pmatrix} \begin{pmatrix} E_{\theta sj} \\ E_{\phi sj} \end{pmatrix},\end{aligned}\quad (20)$$

$S_1 \equiv S_1(\cos \theta_j)$ and $S_2 \equiv S_2(\cos \theta_j)$ are elements of the scattering matrix [31,36] dependent on the wave number k , particle radius a and the complex refraction index m of the particle material, relative to the ambient medium. In Eq. (20), the Cartesian and spherical coordinates are measured in the frame (x, y_j, z_j) associated with the j -th incident plane wave (see Fig. 1). The scattered field is completely transverse: all the components of Eq. (20) are orthogonal to the unit vector \mathbf{e}_R . In the simplest case of the Rayleigh scattering, when the particle is much less than the wavelength,

$$S_1 = -i(ka)^3 \frac{m^2 - 1}{m^2 + 2}, \quad S_2 = S_1 \cos \theta_j; \quad (21)$$

in more general situations, S_1 and S_2 are expressed via the spherical functions. Each plane wave of the incident field is scattered independently, so the resulting scattered field can be found by vector summation of the results obtained from Eqs. (19) and (20). In view of relations (19) and for future convenience, we represent it in the form

$$\mathbf{E}_{sc1} + \mathbf{E}_{sc2} = \mathbf{E}_s \frac{e^{ikR}}{kR}, \quad \mathbf{H}_{sc1} + \mathbf{H}_{sc2} = \mathbf{H}_s \frac{e^{ikR}}{kR}. \quad (22)$$

The auxiliary quantities \mathbf{E}_s and \mathbf{H}_s represent the “meaningful” parts of the scattered field amplitudes – slowly varying envelopes imposed over the standard spherical-wave factor e^{ikR}/kR .

Now, with allowance for Eqs. (10), Eq. (5) can be written as

$$\Delta \mathbf{p} = \frac{g}{ckR} \operatorname{Re} \left[\frac{\mathbf{E}_s^* \times \mathbf{H}_s}{kR} + \mathbf{E}_1^* \times \mathbf{H}_s e^{ik(R-z_1)} + \mathbf{E}_2^* \times \mathbf{H}_s e^{ik(R-z_2)} + \mathbf{E}_s^* \times \mathbf{H}_1 e^{-ik(R-z_1)} + \mathbf{E}_s^* \times \mathbf{H}_2 e^{-ik(R-z_2)} \right] \quad (23)$$

which should be substituted into (6). The first term in brackets describes the momentum of the scattered field and constitutes a separate interest. For further references, it would be suitable to represent its contribution to the ponderomotive force (6) as a sum of two terms that express the momentum flux into the forward $\mathbf{P}(+)$ and backward $\mathbf{P}(-)$ hemispheres, respectively:

$$\mathbf{F}_s = -\frac{g}{n(kR)^2} \oint_{A_R} \mathbf{E}_s^* \times \mathbf{H}_s dA = -\mathbf{P}_s(+)-\mathbf{P}_s(-) \quad (24)$$

where

$$\mathbf{P}_s(\pm) = \frac{g}{\mu k^2} \int_0^{2\pi} d\phi \int_{\pi/4(1\mp 1)}^{\pi/4(3\mp 1)} \left(|E_{\theta s}|^2 + |E_{\phi s}|^2 \right) \mathbf{e}_R(\theta, \phi) \sin \theta d\theta; \quad (25)$$

the latter expression is derived with account for Eqs. (20).

In principle, the “scattering-field force” (24) can be evaluated analytically, at least in the Rayleigh regime when Eqs. (21) hold; however, the presence of two plane waves (10) and the necessity to switch between the three coordinate frames make this way too cumbersome. Fortunately, due to the well developed methods for calculation of the scattering matrix (20) [31], the problem can be easily solved numerically. This is not the case for other terms of Eq. (23) whose numerical integration is practically impossible because of quickly oscillating interference factors $\exp[\pm ik(R-z_j)]$. Nevertheless, their expressions at $R \rightarrow \infty$ can be found analytically via the asymptotic approximation of integral

$$\int_0^\pi U(\theta) e^{\pm ikR(1-\cos \theta)} \sin \theta d\theta = \frac{e^{\pm ikR}}{\mp ikR} \left[e^{\pm ikR} U(\theta)_{\theta=\pi} - e^{\mp ikR} U(\theta)_{\theta=0} \right] + O\left(\frac{1}{k^2 R^2}\right)$$

where $U(\theta)$ is an arbitrary function with sufficiently regular behavior. When applied to summands of (23), this formula gives

$$R^2 \operatorname{Re} \int_0^{2\pi} d\phi_j \int_0^\pi \left[\mathbf{E}_j^* \times \mathbf{H}_s e^{ik(R-z_j)} + \mathbf{E}_s^* \times \mathbf{H}_j e^{-ik(R-z_j)} \right] \sin \theta_j d\theta_j$$

$$= R^2 \frac{2\pi}{kR} \operatorname{Im} \left[e^{2ikR} \left(\mathbf{E}_j^* \times \mathbf{H}_s \right)_{\theta_j=\pi} - \left(\mathbf{E}_j^* \times \mathbf{H}_s \right)_{\theta_j=0} - e^{-2ikR} \left(\mathbf{E}_s^* \times \mathbf{H}_j \right)_{\theta_j=\pi} + \left(\mathbf{E}_s^* \times \mathbf{H}_j \right)_{\theta_j=0} \right]. \quad (26)$$

Further, since $\mathbf{H}_j = \mathbf{e}_{zj} \times \mathbf{E}_j$ and $\mathbf{H}_s = \mathbf{e}_R \times \mathbf{E}_s$, the following relations fulfill:

$$\mathbf{E}_s^* \times \mathbf{H}_j = \mathbf{E}_s^* \times (\mathbf{e}_{zj} \times \mathbf{E}_j) = \mathbf{e}_{zj} (\mathbf{E}_s^* \cdot \mathbf{E}_j) - \mathbf{E}_j (\mathbf{e}_{zj} \cdot \mathbf{E}_s^*),$$

$$\mathbf{E}_j^* \times \mathbf{H}_s = \mathbf{E}_j^* \times (\mathbf{e}_R \times \mathbf{E}_s) = \mathbf{e}_R (\mathbf{E}_j^* \cdot \mathbf{E}_s) - \mathbf{E}_s (\mathbf{e}_R \cdot \mathbf{E}_j^*). \quad (27)$$

Note that in point $\theta_j = 0$ $\mathbf{e}_R = \mathbf{e}_{zj}$, in point $\theta_j = \pi$ $\mathbf{e}_R = -\mathbf{e}_{zj}$ (see Fig. 1). Accordingly, in these points the second summands of Eqs. (27) vanish and

$$\left(\mathbf{E}_j^* \times \mathbf{H}_s \right)_{\theta_j=0} = \left(\mathbf{E}_s^* \times \mathbf{H}_j \right)_{\theta_j=0}^*, \quad \left(\mathbf{E}_s^* \times \mathbf{H}_j \right)_{\theta_j=\pi} = - \left(\mathbf{E}_j^* \times \mathbf{H}_s \right)_{\theta_j=\pi}^*. \quad (28)$$

As a result, contributions of points $\theta_j = \pi$ in expression (26) tend to zero and, combining (26), (28), (23) and (6), one obtains

$$\mathbf{F} = \mathbf{F}_s - g \frac{4\pi}{nk^2} \operatorname{Im} \left[\left(\mathbf{E}_s^* \times \mathbf{H}_1 \right)_{\theta_1=0} + \left(\mathbf{E}_s^* \times \mathbf{H}_2 \right)_{\theta_2=0} \right] \quad (29)$$

where \mathbf{F}_s is given by Eqs. (24) and (25), \mathbf{E}_s is determined by Eqs. (22), (19) and (20), and \mathbf{H}_j is the amplitude of the incident plane-wave component as defined in Eq. (8). Note that due to the accepted incident field geometry (Fig. 1), both summands in brackets of Eq. (29) are vectors belonging to plane (yz), and the x -component of the total force exerted on the particle, $F_x = F_{xs}$, is fully determined by the scattered-field force (24).

III. MECHANICAL PROPERTIES OF THE SCATTERED FIELD

The model described by Eqs. (9) and (11) – (18) is applicable to a number of practical situations involving the incident fields with inhomogeneous amplitude-phase profile and polarization [27]. For the detailed analysis, we choose the simplest configurations which enable to analyze the special features of the SFD and TFD [26]. The first example is realized in the symmetric superposition of circularly polarized plane waves (9) that appears if

$$\gamma_1 = -\gamma_2 = \gamma, \quad (30)$$

$$\begin{pmatrix} E_{x1} \\ E_{y1} \end{pmatrix} = E_0 \begin{pmatrix} 1 \\ \sigma i \end{pmatrix} \quad (31)$$

and both waves are identical with possible phase shift, i.e.

$$\begin{pmatrix} E_{x2} \\ E_{y2} \end{pmatrix} = \exp(i\delta) \begin{pmatrix} E_{x1} \\ E_{y1} \end{pmatrix} \quad (32)$$

where $\sigma = \pm 1$ is the polarization helicity (spin number). In the paraxial case ($\gamma \ll 1$), to which we are restricted in this paper, terms $\sim \gamma^2$ and higher can be neglected, and Eqs. (11) – (18) reduce to [26]

$$w = 4\varepsilon g |E_0|^2 (1 + \cos 2\Phi), \quad (33)$$

$$p_{sx} = -\frac{4g_e}{c} \sigma \gamma |E_0|^2 \sin 2\Phi, \quad (34)$$

$$p_{sy} = p_{sz} = p_{oy} = p_{ox} = 0,$$

$$p_{oz} = \frac{4g_e}{c} |E_0|^2 (1 + \cos 2\Phi) \quad (35)$$

with

$$\Phi = \gamma ky - \frac{\delta}{2}. \quad (36)$$

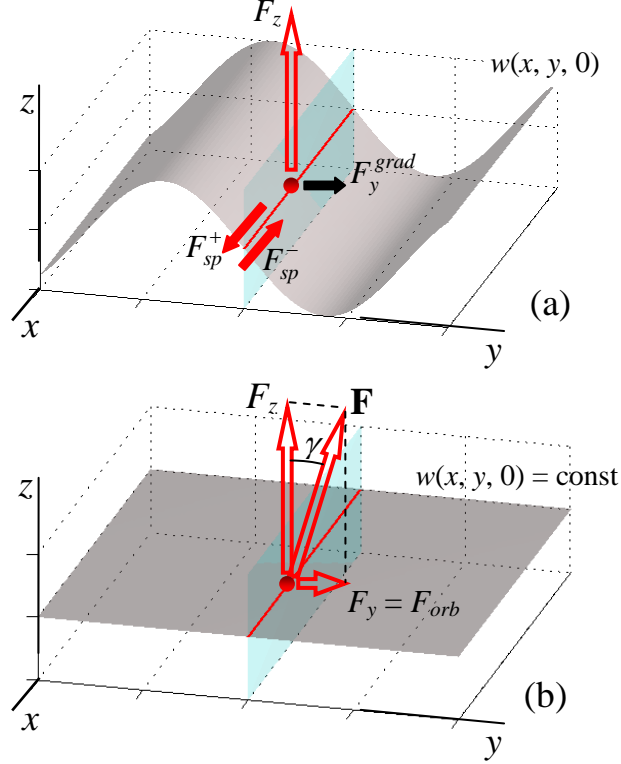


Fig. 2. Mechanical forces acting on a probe particle situated in plane $z = 0$ and illuminated by the superposition of two plane waves with (a) different directions, resulting in the inhomogeneous circularly polarized field described by Eqs. (30) – (35) and (b) coinciding directions, resulting in the spatially homogeneous energy distribution but inclined wavefront, according to Eqs. (44), (45). Further explanations see in text.

These equations characterize the field with inhomogeneous energy distribution over the reference plane $z = 0$ [Fig. 2(a)]. The OFD (35) of this field is directed along the propagation axis z (is completely longitudinal); the internal OFD is absent. As should be expected under the paraxial conditions [12], the longitudinal momentum (35) and the energy density (33) are connected by the standard relation $p_z = nw/c$. The longitudinal momentum produces the usual light pressure force F_z pushing the particle forward; the inhomogeneous intensity is the source of the gradient force F_y^{grad} [(see Fig. 2(a)] that was analyzed elsewhere [26]. Both these forces are not the subjects of our present consideration; instead, we intend to concentrate on the transverse SFD (34) which represents the most interesting feature of the discussed field model. The very appearance of the x -directed transverse momentum in this field geometry seems counter-intuitive, though it immediately follows from the spin flow theory [7] and is quite expectedly [9,12] oriented along the constant-energy lines $y = \text{const}$.

Its physical nature is partially elucidated by considering the scattering field momentum flux behavior with growing the particle size parameter

$$\xi = ka \quad (37)$$

where a is the particle radius. We calculated the scattered field parameters of Eqs. (24), (25) for two sorts of spherical particles suspended in water ($\varepsilon = 1.77$, $\mu = 1$, $n = 1.33$): metallic (gold in water, relative refraction index $m = 0.32 + 2.65i$ [36]), and dielectric (latex in water, $m = 1.12$); the radiation wave number is chosen $k = 1.33 \cdot 10^5 \text{cm}^{-1}$ (He-Ne laser). The results obtained for the field model of Eqs. (30) – (32) are given by curves $P_{sx}^+(\pm)$ in Fig. 3; note that only results for the field model with $\sigma = +1$ in Eq. (31) are presented because switching the polarization helicity to $\sigma = -1$ causes nothing but the sign reversal, $P_{sx}^-(\pm) = -P_{sx}^+(\pm)$. For comparison, in Fig. 3 the results are also presented that were obtained for different cases of the linearly polarized incident beam, which occur if, instead of Eq. (31), the following relations take place:

$$E_{y1} = 0, E_{x1} = E_0 \neq 0 \quad (38)$$

(“x-polarization”, curves $P_{sx}^x(\pm)$ and $P_{sy}^x(\pm)$),

$$E_{x1} = 0, E_{y1} = E_0 \neq 0 \quad (39)$$

(“y-polarization”, curves $P_{sx}^y(\pm)$ and $P_{sy}^y(\pm)$), and

$$E_{y1} = E_{x1} = E_0 \neq 0 \quad (40)$$

(“45° polarization”, curves $P_{sx}^{45}(\pm)$ and $P_{sy}^{45}(\pm)$). Upon calculations, condition

$$2\Phi = -\pi/2 \quad (41)$$

($y = 0$, $\delta = \pi/2$ or $\delta = 0$, $y = \pi/(4k\gamma)$) was chosen that corresponds to maximum absolute value of the spin flow (34); the angle between the two interfering plane waves was assumed to be equal

$$\gamma = 0.01 \text{ rad}. \quad (42)$$

To eliminate the influence of the incident beam intensity and to decrease the range of presented data, they are normalized by means of dividing the calculated quantities by the total momentum flux of the incident field through the particle cross section,

$$P_0 = \frac{2g}{\mu} \left(|E_{x1}|^2 + |E_{y1}|^2 \right) \cdot \pi a^2. \quad (43)$$

Additionally, in Fig. 3 a non-linear vertical scale is used so that the real deviations of the data points from the zero line are proportional to the fourth root of the corresponding momentum flux value.

Curves $P_{sx, sy}^{++}(\pm)$ and $P_{sx, sy}^{--}(\pm)$ in Fig. 3 represent the transverse Cartesian components of the front and rear half-sphere momentum fluxes calculated via Eq. (25) in differently polarized fields. In usual conditions, in the small-particle limit (Rayleigh scattering regime [31]), the scattering is considered symmetric, in agreement with Eqs. (21). This implies that the scattered radiation carries no transverse momentum flux; and really, for linearly polarized incident light, results of Fig. 3 confirm this suggestion with rather high accuracy at least until $\xi = 0.2$, where the particle size influence becomes perceptible. Even beyond this range limit, the forward and backward scattered momentum fluxes are close to each other for all cases with linearly polarized incident field presented in Fig. 3.

However, when the particle is illuminated by the circularly polarized light, both the forward- and backward-scattered momentum fluxes possess noticeable x -directed components [curves $P_{sx}^+(\pm)$ in Figs. 3(a), (b)], much more intense than any analogous contribution emerging under the linearly-polarized illumination. According to Fig. 3 and with allowance for the normalization factor (43), quantities $|P_{sx}^+(\pm)|$ grow as a^6 with the particle size, which is of the same order as the total scattered intensity is [31], and which strongly exceeds all other factors causing the scattered field

anisotropy. Besides, the forward $P_{sx}^+(+)$ and backward $P_{sx}^+(-)$ transverse momentum fluxes essentially differ, even by the sign. These effects can be attributed to the optical vortex generation (spin-to-orbital angular momentum conversion) upon scattering of light with circular polarization [37,38], which directly follows from Eqs. (20) and (21). In the laboratory frame, the fore-scattered and back-scattered vortices possess opposite spiralities, and this is the source of the scattering asymmetry. For a single incident plane wave, this asymmetry is “hidden” in the hemisphere momentum fluxes due to integration over the azimuth angle ϕ in Eq. (25) but interference of the scattered fields produced by the two plane waves makes it visible. One can expect the revealed forward-backward asymmetry to be a general feature inherent in scattering of any spatially inhomogeneous elliptically polarized beams in the Raleigh scattering regime [26]. This effect can be considered as a novel manifestation of the spin-orbit interaction upon the light scattering, whose observation requires the spatially inhomogeneous incident field.

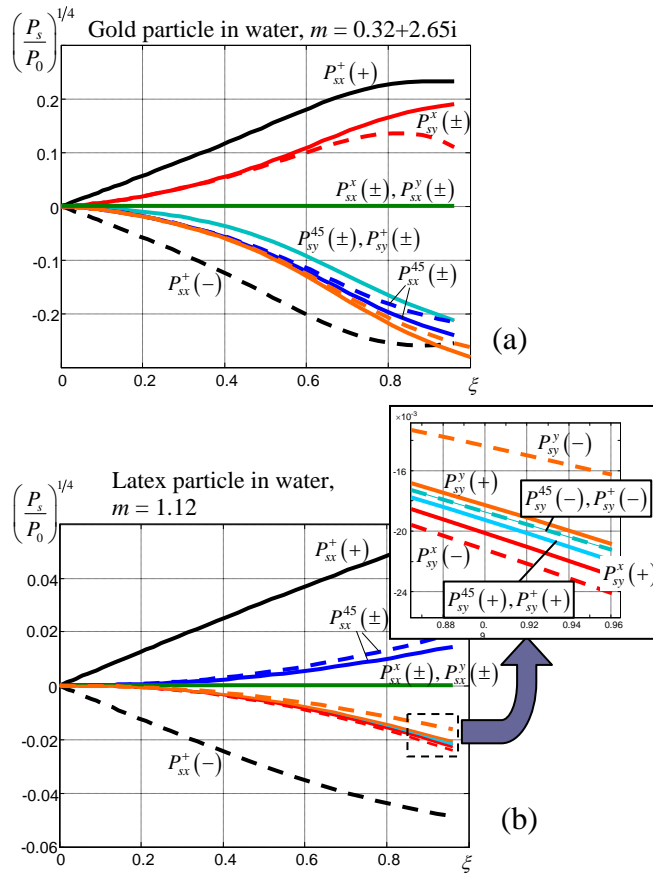


Fig. 3. Fourth root of the normalized momentum flux \mathbf{P}_s/P_0 [see Eqs. (25) and (43)] components of the field scattered by a spherical (a) metallic and (b) dielectric particle, suspended in water, vs the particle size parameter (37), calculated for conditions of Eqs. (41), (42). Each curve is marked by the corresponding component notation: subscripts (x, y) denote the momentum flux Cartesian component, superscripts (x, y, 45, +) denote the incident field polarization as indicated by Eqs. (31) and (38) – (40). Solid (dashed) lines describe the momentum flux into the forward (backward) hemisphere; the inset shows magnification of the dashed rectangle in panel (b). In both cases (a) and (b), curves $P_{sx}^x(\pm)$ and $P_{sx}^y(\pm)$ coincide with the zero line, curves $P_{sx}^{45}(\pm)$ and $P_{sx}^+(-)$ visually merge (however, the small difference between the forward and backward scattered contributions can be traced in the inset).

What is even more important, the absolute values of $P_{sx}^+(+)$ and $P_{sx}^+(-)$ are not exactly the same, and their difference is just the source of the “net” scattered field momentum flux that can be determined via Eq. (24). This momentum flux is “balanced” by the recoil force exerted on the particle – the physical reason for the translational ponderomotive influence of the inhomogeneous circularly polarized optical field, which can be treated as the mechanical action of the spin energy flow [26]. The comparative study of this mechanical action is the subject of next Section.

IV. COMPARISON OF THE MECHANICAL ACTIONS OF THE SPIN AND ORBITAL ENERGY FLOWS

In this section, we apply the general procedure formulated in Section IIB, Eqs. (24), (25) and (29), to calculation of the mechanical forces exerted on the probe particles and confront it with the energy flow pattern in the incident circularly polarized field. Recently, this procedure was described in detail [26], and now we follow it with no essential modifications.

An impressive feature of the calculated results is the “counter-intuitive” x -directed force represented by curves F_{sp}^\pm in Fig. 4(a), (b) and arrows F_{sp}^\pm in Fig. 2(a): apparently, the field configuration of Eqs. (8) – (10) and (30) – (32) looks symmetric with respect the x -axis reversal, and it is the “invisible” instant field vector rotation that destroys this symmetry. Moreover, this force changes the sign upon switching the polarization handedness and vanishes in linearly polarized fields¹ [which directly follows from near-zero values of the partial momentum fluxes $P_{sx}^x(\pm)$, $P_{sx}^y(\pm)$ presented in Fig. 3(a), (b)]. All this is akin to the behavior of the SFD (34) which, in accordance with Eqs. (33) – (35), represents the only x -directed energy flow contribution emerging in the incident field specified by Eqs. (30) – (32); besides, there is no energy gradient in the x -direction. That is why it is quite natural to associate the x -directed force F_{sp}^\pm with the SFD of the incident field and consider it as the mechanical action of the spin energy flow.

The next step is to compare this force with the orbital flow action. Unfortunately, in the field that satisfies Eqs. (30) – (32), the transverse OFD is absent, and the really existing y -directed force [Fig. 2(a)] was identified as the gradient force [26], which is useless for our purpose of analyzing the mechanical action owing to the internal energy flows. To avoid this inconvenience, one could address more complex field configurations in which the orbital and spin internal flows are present simultaneously (see, e.g., Refs. [9,10]). However, in such situations not only the force calculation will be much more cumbersome and time-expensive, but also interpretation of the numerical results and separation between the SFD-induced and OFD-induced force contributions becomes rather difficult.

More promising way is to find a simple field configuration in which the OFD-induced action F_{orb} can be easily identified, and its correspondence with the orbital flow distribution can be established. If, additionally, the local OFD value is numerically equal to the SFD in the model of Eqs. (31) – (36), then the calculated forces F_{orb} and F_{sp}^\pm can be treated as “pure” manifestations of the orbital and spin flow mechanical actions, respectively. The fact that F_{orb} and F_{sp}^\pm are realized in different optical fields, is not important because, if there exist any regularities of the ponderomotive effects immanently inherent in the SFD (OFD) ‘per se’, their manifestations should be identical provided that the local SFD (OFD) values are the same, regardless of all other field parameters and details.

Formally, a simple configuration with obviously identifiable OFD action can be realized on the base of the same two-plane-wave field of Eqs. (10) – (18). All one must do is to accept, in contrast to Eq. (30), the condition

¹ In fact, when the incident field linear polarization differs from “pure” x - or y -polarization, the specific x -directed force appears but it is not related to any energy flow constituent and can be attributed to the polarization inhomogeneity [26].

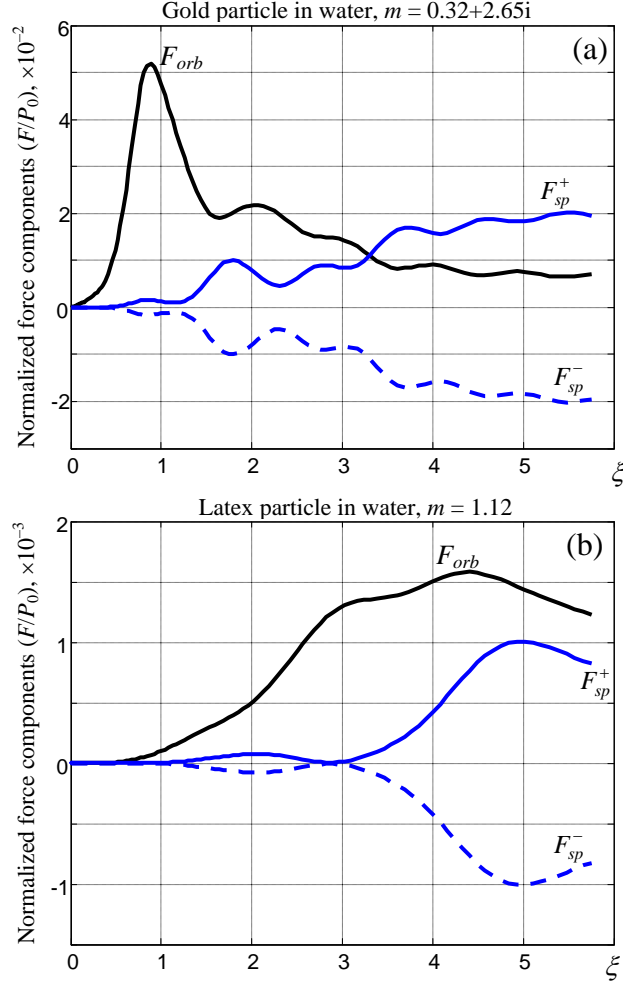


Fig. 4. Comparison of the mechanical actions associated with the spin and orbital internal energy flows for (a) metal and (b) dielectric spherical particle suspended in water. Each curve represents the force dependence of the particle size parameter (37). The SFD-induced forces F_{sp}^{\pm} are calculated as x -components of the force experienced by a particle in the field characterized by Eqs. (30) – (36) in conditions of Eqs. (41), (42) [cf. Fig. 2(a)]; it changes the sign upon switching the polarization handedness from $\sigma = 1$ (solid lines) to $\sigma = -1$ (dashed lines). The OFD-induced contributions F_{orb} are determined as y -components of the force exerted on a particle in the field characterized by Eqs. (44) and (41), (42) [cf. Fig. 2(b)].

$$\gamma_1 = \gamma_2 = \gamma. \quad (44)$$

Then the SFD vanishes, the whole transverse momentum is of the orbital nature and equals

$$p_{Oy} = \frac{4g_e}{c} \gamma |E_0|^2 (1 + \cos 2\Phi) \quad (45)$$

which exactly coincides with Eq. (34) and means that, keeping the same values of γ , E_0 and Φ , the y -directed OFD (45) in the field configuration of Eqs. (44), (31) and (32) equals to the x -directed SFD (34) in the field configuration of Eqs. (30) – (32). Hence, one can testify the equivalence and/or discrepancies between mechanical actions of the spin and orbital energy flows merely by juxtaposing the x -directed force F_{sp}^{\pm} calculated as described above, and the y -directed force F_{orb} calculated for the incident field configuration specified by Eqs. (44), (31) and (32).

One may notice that condition (44) reduces the two-plane-wave superposition to the case of a single plane wave that approaches the nominal observation plane $z = 0$ at a small angle γ . In this

field, the energy is distributed homogeneously and the OFD (45) is, in fact, the transverse projection of the plane-wave momentum directed normally to the wavefront [Fig. 2(b)]. This circumstance does not limit generality of the consideration: it complies with the common notion that the OFD represents the transverse energy transportation of the same nature as the “main” longitudinal energy flow [12], and that the OFD-induced mechanical action is nothing but a sort of the transverse light pressure. Such origination of the transverse ponderomotive action is reflected in Fig. 2(b) by decomposition of the light-pressure vector \mathbf{F} into the longitudinal F_z and transverse $F_y = F_{orb}$ components.

In view of the above remarks, the specific features of the SFD- and OFD-induced mechanical actions can be investigated via the comparative analysis of curves F_{sp}^\pm and F_{orb} in Figs. 4a, b. The first and quite expected difference between them is that, both for metallic [Fig. 4(a)] and dielectric [Fig. 4(b)] particles, the spin-flow contribution changes the sign together with the polarization handedness (curves F_{sp}^+ and F_{sp}^-) while the orbital flow action does not. In all other aspects, similarities and discrepancies of them are not seen so immediately. Both the spin- and orbital-flow actions depend on the particle size and optical properties; in particular, conditions are possible when one of the discussed contributions is strongly prevailing: for example, very small particles ($\xi \ll 1$) “feel” the OFD much better than the SFD; also, the spin-induced force F_{sp}^\pm practically vanishes at certain moderate particle sizes, as is seen near the point $\xi = 2.8$ in Fig. 4(b). Probably, difference in the F_{sp}^\pm and F_{orb} dependences on ξ can be used for the separate detection of the spin and orbital energy flows.

Curves in Fig. 4 demonstrate the general rule that any light field mechanical action is essentially mediated by the probe particle size and properties. In this context, the results for very small particles are more representative since their dependence on the particle size and refraction index is more regular and is not modified by the resonance phenomena [31]. The corresponding data are presented in Fig. 5. Among other things, they reveal the difference between the OFD action exerted on the dielectric ($F_{orb} \sim a^6$) and the metallic ($F_{orb} \sim a^3$) particles. This can be explained by prevailing role of the light absorption in the light-pressure effect on conductive particles whereas the OFD-induced action experienced by a dielectric particle owes completely to the elastic scattering [31]; the same reason (together with the small relative refraction index) underlies the appreciably lower absolute values of forces in case of dielectric particles (cf. the vertical scales in Figs. 4a and 4b). Another important observation concerns the peculiar regularity of the SFD-induced action which for both considered cases satisfies the relation $F_{sp}^\pm \sim a^8$. Undoubtedly, this feature is related to the special mechanism of the SFD-induced ponderomotive effect and reflects its particular physical nature.

Interestingly, in the dipole approximation [28,34], the whole mechanical action experienced by Rayleigh particles consists of the gradient force (first summand of Eq. (5) of Ref. [34]) and the OFD-induced force (the “scattering force” – second summand of the mentioned Eq. (5) of [34] – is proportional to the “electric” part of the OFD, without restoring the “electric-magnetic democracy” [10]). In fact, the “field gradient force” introduced by Eqs. (6) and (8) of [34] expresses the inverse SFD-induced action which is subtracted from the “dissipative radiation force” of Eq. (7), Ref. [34]. In this context, the particle-size dependence of the OFD-induced forces seen in Fig. 5 ($\sim a^3$ for conductive and $\sim a^6$ for dielectric particles) is completely justified by the behavior of imaginary part of the polarizability for absorbing and non-absorbing particles (Eq. (11) of [34]).

The eighth degree in the particle-size dependence testifies that the SFD-induced mechanical action is not of the dipole nature and only appears in higher degrees of the multipole expansion. Note however that the relative weakness of the spin-flow force in the Rayleigh-scattering region

does not mean that it is always smaller than the orbital-flow one: as Fig. 4 testifies, at $\xi \sim 1$, both forces are quite commensurable, and even $|F_{sp}^\pm|$ may exceed F_{orb} .

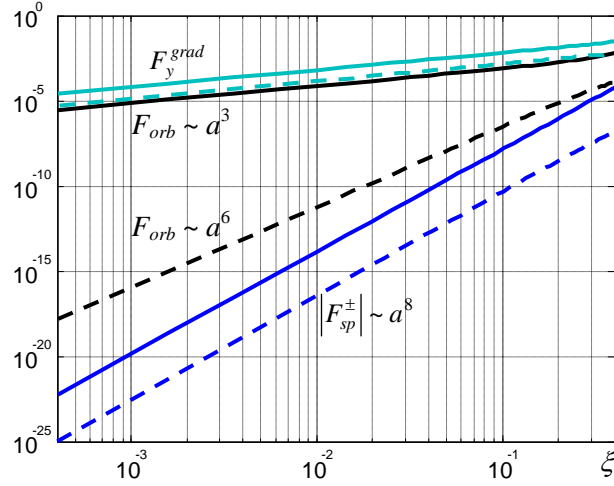


Fig. 5. Initial segments of curves, presented by Fig. 4, in the double logarithmic scale. Solid lines: metallic particle [Fig. 4(a)], dashed lines: dielectric particle [Fig. 4(b)]. Orders of the force growth with the particle radius a are indicated with allowance for the normalization factor P_0 (43). For comparison, behavior of the gradient force F_y^{grad} [Fig. 2(a)] is also illustrated.

In view of these facts, recent suggestions on the mechanical equivalency of the spin and orbital energy flows [26] should be essentially corrected, unless rejected. Really, both the spin and orbital constituents of the energy flow are able to cause translational motion of the probe particles but quantitative characters of the spin-induced and the orbital-induced motions and their dependences on the particle size and properties are rather different. Accordingly, the SFD and OFD can be distinguished in experiments employing probe particles with specially chosen sizes and properties. Such a choice requires the detailed analysis of expected behavior of various sorts of particles, which can be performed, for example, on the base of the approach presented in this paper.

V. CONCLUSION

The results of this work are based on the model of spatially inhomogeneous optical field [26] that is formed by superposition of two plane waves. Despite its simplicity, the model adequately represents some general properties of inhomogeneous fields, including the main regularities inherent in internal energy flow and its spin and orbital parts. By using the Mie theory, mechanical characteristics of the field scattered by a probe particle placed within the spatially inhomogeneous circularly polarized light beam are studied. In particular, the forward – backward scattering field asymmetry, observable in the Rayleigh scattering regime (for particle sizes much less the radiation wavelength) and associated with the spin energy flow of the incident beam, has revealed and analyzed. This spin-flow induced asymmetry is closely related to the known effect of the spin-orbital angular momentum conversion upon the Rayleigh scattering [37,38] and can be treated as a novel manifestation of the spin-orbit interaction of light.

By means of numerical calculations, the ponderomotive forces exerted on spherical microparticles with conductive and dielectric properties, exposed to light fields with different configurations, are also investigated. The two specific incident field configurations were considered in detail: (i) spatially inhomogeneous beam with the well-defined transverse spin flow and (ii) spatially homogeneous field with the transverse orbital flow (inclined plane wave). Comparison of

the ponderomotive actions, performed in both cases, permitted us to disclose the special features of the mechanical action inherent in the spin and orbital parts of the internal energy flow. In particular, for the subwavelength (Rayleigh) particles, the orbital-flow force grows as a^3 for conducting and as a^6 for dielectric particle with radius a , in compliance with the dipole interaction mechanism [28,34]; the spin-flow force appears in higher multipole orders and behaves as a^8 in both cases. This difference reflects peculiar ways in which the spin and orbital momenta of light are transmitted to material bodies, in particular, the essential role of non-dipole interactions in the spin flow mechanical action.

We hope that the results of this work can be useful for experimental identification and separate investigation of the spin and orbital parts of the internal energy flow in light fields via the probe particle's motion. Simultaneously, our results indicate some difficulties and limitations of approaches based on the ponderomotive action and probe bodies. First to note, there is a number of "parasite" sources of mechanical influences that are not related with the field momentum or any of its constituents and usually mask their contributions. Among various factors mentioned in the Introduction, here we stress upon the non-Poynting source of the electromagnetic origin, that plays important role in any inhomogeneous light field – the gradient force. According to Fig. 5, lines F_y^{grad} , it, generally, exceeds the energy-flow-induced contributions, and this circumstance should be properly addressed in any experiment (see also Refs. [26,28,29]). Another essential issue is that beyond the Rayleigh-scattering range of the probe particle sizes, the electromagnetic field-induced mechanical action depends on the particle radius and on the complex refraction index in a rather complex and apparently irregular fashion, strongly affected by the field inhomogeneity, and this makes it very difficult to establish an accurate numerical correspondence between the transverse ponderomotive force and the internal energy flow component which, theoretically, gives rise to this force. In most cases the resulting force value is rather far from naïve expectations that the mechanical action is proportional to the local value of the incident field momentum density in the point where the particle is placed [26]. In essence, in such situations not the field momentum (energy flow) 'per se' but the electromagnetic field as a whole acts as a motive power, and it seems doubtful that the observable force experienced by a particle can be definitely associated with the transverse field momentum at all.

Finally, we emphasize that the model of inhomogeneous optical field described in this paper, even in its simplest version, provides consistent deductions relating the mechanical actions of spatially inhomogeneous vector light fields. The presented model can be easily generalized to describe more complicated situations to reflect additional fine features of the real optical fields.

References

1. L. Allen, M. J. Padgett, M. Babiker, Orbital angular momentum of light, *Prog. Opt.* **39**, 291–372 (1999).
2. M. S. Soskin and M. V. Vasnetsov, Singular optics, *Prog. Opt.* **42**, 219–276 (2001).
3. A. Ya. Bekshaev, M. S. Soskin, M. V. Vasnetsov, *Paraxial Light Beams with Angular Momentum* (Nova Science Publishers, New York, 2008).
4. M. R. Dennis, K. O'Holleran, M. J. Padgett, Singular optics: optical vortices and polarization singularities, *Prog. Opt.* **53**, 293–364 (2009).
5. L. Allen and M. J. Padgett, The Poynting vector in Laguerre-Gaussian beams and the interpretation of their angular momentum density, *Opt. Commun.* **184**, 67–71 (2000).
6. V. A. Pas'ko, M. S. Soskin, and M. V. Vasnetsov, Transversal optical vortex, *Opt. Commun.* **198**, 49–56 (2001).
7. A. Ya. Bekshaev, Spin angular momentum of inhomogeneous and transversely limited light beams, *Proc. SPIE* **6254**, 625407 (2006).
8. I. I. Mokhun, Introduction to linear singular optics, in *Optical correlation techniques and applications*, 1–132 (SPIE Press PM168, Bellingham, 2007).

9. A. Ya. Bekshaev and M. S. Soskin, Transverse energy flows in vectorial fields of paraxial beams with singularities, *Opt. Commun.* **271**, 332–348 (2007).
10. M. V. Berry, Optical currents, *J. Opt. A: Pure Appl. Opt.* **11**, 094001 (2009).
11. K. Y. Bliokh, M. A. Alonso, E. A. Ostrovskaya, and A. Aiello, Angular momenta and spin-orbit interaction of non-paraxial light in free space, *Phys. Rev. A* **82**, 063825 (2010).
12. A. Bekshaev, K. Bliokh, and M. Soskin, Internal flows and energy circulation in light beams, *J. Opt.* **13**, 053001 (2011).
13. M. A. Seo, A. J. L. Adam, J. H. Kang, J. W. Lee, S. C. Jeoung, Q. H. Park, P. C. M. Planken, and D. S. Kim, Fourier-transform terahertz near-field imaging of one-dimensional slit arrays: mapping of electric-field-, magnetic-field-, and Poynting vectors, *Opt. Express* **15**, 11781–11789 (2007).
14. T. Zentgraf, J. Dorfmüller, C. Rockstuhl, C. Etrich, R. Vogelgesang, K. Kern, T. Pertsch, F. Lederer, and H. Giessen, Amplitude- and phase-resolved optical near fields of split-ring-resonator-based metamaterials, *Opt. Lett.* **33**, 848–850 (2008).
15. A. Bitzer, H. Merbold, A. Thoman, T. Feurer, H. Helm, and M. Walther, Terahertz near-field imaging of electric and magnetic resonances of a planar metamaterial, *Opt. Express* **17**, 3826–3834 (2009).
16. N. Fang and X. Zhang, Imaging properties of a metamaterial superlens, *Appl. Phys. Lett.* **82**, 161–163 (2003).
17. A. Ya. Bekshaev, Oblique section of a paraxial light beam: criteria for azimuthal energy flow and orbital angular momentum, *J. Opt. A: Pure Appl. Opt.* **11**, 094003 (2009).
18. C.-C. Chen and J. F. Whitaker, An optically-interrogated microwave-Poynting vector sensor using cadmium manganese telluride, *Opt. Express* **18**, 12239–12248 (2010).
19. R. Khrobatin, I. Mokhun, and J. Viktorovskaya, Potentiality of experimental analysis for characteristics of the Poynting vector components, *Ukr. J. Phys. Opt.* **9**, 182–186 (2008).
20. M. Dienerowitz, M. Mazilu, and K. Dholakia, Optical manipulation of nanoparticles: a review, *Journal of Nanophotonics* **2**, 021875 (2008).
21. A. T. O’Neil, I. MacVicar, L. Allen, and M. J. Padgett, Intrinsic and extrinsic nature of the orbital angular momentum of a light beam, *Phys. Rev. Lett.* **88**, 053601 (2002).
22. V. Garcés-Chavez, D. McGloin, M. D. Summers, A. Fernandez-Nieves, G. C. Spalding, G. Cristobal, and K. Dholakia, The reconstruction of optical angular momentum after distortion in amplitude, phase and polarization, *J. Opt. A: Pure Appl. Opt.* **6**, S235–S238 (2004).
23. Y. Zhao, J. S. Edgar, G. D. M. Jeffries, D. McGloin, and D. T. Chiu, Spin-to-orbital angular momentum conversion in a strongly focused optical beam, *Phys. Rev. Lett.* **99**, 073901 (2007).
24. J. D. Jackson, *Classical Electrodynamics* (Wiley, New York, 1999).
25. A. Ashkin, *Optical Trapping and Manipulation of Neutral Particles Using Lasers* (World Scientific, NJ, 2006).
26. A. Ya. Bekshaev, O. V. Angelsky, S. V. Sviridova, and C. Yu. Zenkova, Mechanical action of inhomogeneously polarized optical fields and detection of the internal energy flows, *Advances in Optical Technologies* **2011**, 723901 (2011).
27. O. V. Angelsky, M. P. Gorsky, P. P. Maksimyak, A. P. Maksimyak, S. G. Hanson, and C. Yu. Zenkova, Investigation of optical currents in coherent and partially coherent vector fields, *Opt. Express* **19**, 660–672 (2011).
28. V. Wong and M. Ratner, Gradient and nongradient contributions to plasmon-enhanced optical forces on silver nanoparticles, *Phys. Rev. B* **73**, 075416 (2006).
29. S. Albaladejo, M. I. Marques, M. Laroche, and J. J. Saenz, Scattering forces from the curl of the spin angular momentum of a light field, *Phys. Rev. Lett.* **102**, 113602 (2009).
30. L. I. Mandelstam, *Lectures on optics, relativity and quantum mechanics* (Nauka, Moscow, 1972) (In Russian).

31. C. F. Bohren and D. R. Huffman, *Absorption and scattering of light by small particles* (Wiley, New York, 1983)
32. O. V. Angelsky, A. Ya. Bekshaev, P. P. Maksimyak, A. P. Maksimyak, S. G. Hanson, and C. Yu. Zenkova, Orbital rotation without orbital angular momentum: mechanical action of the spin part of the internal energy flow in light beams, *Opt. Express* **20**, 3563–3571 (2012).
33. O. V. Angelsky, A. Ya. Bekshaev, P. P. Maksimyak, A. P. Maksimyak, I. I. Mokhun, S. G. Hanson, C. Yu. Zenkova, and A. V. Tyurin, Circular motion of particles suspended in a Gaussian beam with circular polarization validates the spin part of the internal energy flow, *Opt. Express* **20** (2012, to appear).
34. S. H. Simpson and S. Hanna, Orbital motion of optically trapped particles in Laguerre–Gaussian beams, *J. Opt. Soc. Am. A* **27**, 2061–2071 (2010).
35. K. Y. Bliokh, F. Nori, Does a Surface Polariton Have Spin? (2012), e-print [arXiv:1201.2746](https://arxiv.org/abs/1201.2746) [physics.optics].
36. H. C. Van de Hulst, *Light scattering by small particles* (Chapman & Hall, New York, 1957).
37. C. Schwartz and A. Dogariu, Conservation of angular momentum of light in single scattering *Opt. Express* **14**, 8425–8433 (2006).
38. K. Y. Bliokh, E. A. Ostrovskaya, M. A. Alonso, O. G. Rodríguez-Herrera, D. Lara, and C. Dainty, Spin-to-orbital angular momentum conversion in focusing, scattering, and imaging systems, *Opt. Express* **19**, 26132–26149 (2011).